



**HAL**  
open science

## A virtual chemistry model for soot prediction in flames including radiative heat transfer

Hernando Maldonado Colmán, Alberto Cuoci, Nasser Darabiha, Benoit Fiorina

► **To cite this version:**

Hernando Maldonado Colmán, Alberto Cuoci, Nasser Darabiha, Benoit Fiorina. A virtual chemistry model for soot prediction in flames including radiative heat transfer. *Combustion and Flame*, 2022, 238, pp.111879. 10.1016/j.combustflame.2021.111879 . hal-03542794

**HAL Id: hal-03542794**

**<https://centralesupelec.hal.science/hal-03542794>**

Submitted on 25 Jan 2022

**HAL** is a multi-disciplinary open access archive for the deposit and dissemination of scientific research documents, whether they are published or not. The documents may come from teaching and research institutions in France or abroad, or from public or private research centers.

L'archive ouverte pluridisciplinaire **HAL**, est destinée au dépôt et à la diffusion de documents scientifiques de niveau recherche, publiés ou non, émanant des établissements d'enseignement et de recherche français ou étrangers, des laboratoires publics ou privés.

# A virtual chemistry model for soot prediction in flames including radiative heat transfer

Hernando Maldonado Colmán<sup>a,\*</sup>, Alberto Cuoci<sup>b</sup>, Nasser Darabiha<sup>a</sup>, Benoît Fiorina<sup>a</sup>

<sup>a</sup>*Laboratoire EM2C, CNRS, CentraleSupélec, Université Paris-Saclay, 3, rue Joliot Curie, 91192 Gif-sur-Yvette, France*

<sup>b</sup>*CRECK Modeling Lab, Department of Chemistry, Materials and Chemical Engineering "G. Natta", Politecnico di Milano, P.zza Leonardo da Vinci 32, 20133 Milano, Italy*

---

## Abstract

Modeling soot formation is a very difficult task which has been assessed by the numerical combustion community. Numerical simulations of turbulent sooting flames remain very challenging due to the complexity of soot formation phenomena, which implies development of elaborate soot models often too computationally demanding, or simplified soot models that are limited to a small range of operating conditions of interest. Here an innovative optimized global approach called virtual chemistry is proposed. It consists of a mathematical formalism including virtual species and virtual reactions, whose thermochemical parameters are optimized in order to describe a combustion system. Thermochemical properties are trained through a genetic algorithm, employing a learning database made of reference flame elements. This makes it possible to reproduce multiple combustion regimes and operating conditions. The virtual chemistry approach reproduces then

---

\*Corresponding author:

*Email address:* `hernando.maldonado-colman@centralesupelec.fr` (Hernando Maldonado Colmán)

the structure of hydrocarbon-air flames, as well as predicting specific user-defined pollutant species. The objective of this article is to extend the virtual chemistry methodology for soot formation prediction. As the radiative heat losses are important in sooting flames, a new radiative virtual model is also developed to account for them. The final reduced chemistry consists of 12 virtual species and 6 virtual reactions considerably decreasing the computational time compared to detailed chemistry models. Simulations of 1-D and 2-D laminar ethylene-air sooting flames are performed to evaluate the virtual soot and radiative models. Temperature, soot volume fraction and radiative heat losses are well predicted and are in good agreement with the reference data.

*Keywords:*

Kinetic modeling; Soot; Radiative heat transfer; Laminar flames

---

## 1. Introduction

Hydrocarbon/air combustion occurring in rich and incomplete conditions in practical industrial applications causes the formation of undesirable soot particles. Soot formation results from both highly complex gas phase chemistry and particles dynamics including nucleation, condensation, coalescence, and surface reactions such as surface growth and oxidation. Because of the complexity of these physico-chemical phenomena, numerical computations of gas chemistry together with particles dynamics request high amounts of CPU time, which quickly become an issue for the simulation of practical combustion chambers.

The chemical kinetics describing the gaseous phase evolution including

soot precursors needs a large number of species and reactions [1] so that detailed chemical mechanisms generally cannot be directly employed in CFD of sooting flames. Three main routes for kinetics reduction techniques are in principle possible [2, 3]: analytically-reduced chemistry, tabulated chemistry and optimized global chemistry. Thanks to recent progresses in computational resources and in the automation of chemistry reduction techniques [4], analytically-reduced schemes have been recently used for LES of turbulent sooting flames [5, 6]. Despite impressive results, the remaining high number of species and the numerical stiffness of the system make difficult the systematic use of analytic schemes in a practical combustion chamber design process. Application of tabulated chemistry to soot formation is therefore more popular. It consists in storing complex chemistry up to polycyclic aromatic hydrocarbons (PAHs) in look-up tables, parametrized by a reduced set of thermochemical variables [7, 8]. Despite its very low CPU cost, the tabulated chemistry approach is not able to well predict multi-regime combustion [9]. Finally, literature presents a few attempts to optimize global mechanisms to predict soot precursor formation [10–12]. In these studies, a global mechanism is adopted to describe the gas chemistry and soot formation is described using a simplified chemistry.

The complex interaction between reactive gas phase and solid particles dynamics has motivated the development of a wide variety of mathematical approaches such as (sorted from high to low computational demand): Lagrangian models [6, 13], Chemical Discrete Sectional Model (CDSM) [1, 14, 15], Aerosol Discrete Sectional model (ADSM) [8, 16–19], or Method of moments (MOMs) [20–23]. In addition, empirical and semi-empirical meth-

ods [10, 24–26] have also been developed to track the soot volume fraction and particle number density, and eventually the particle size distribution [27]. Such pragmatic approaches are attractive because of their very low CPU cost, but in contrast, they are limited to a small range of operating conditions. In most cases, the parameters are a function of the fuel. New techniques using machine learning algorithms, such as artificial neural networks (ANNs), have been recently developed to tackle the soot prediction problem by using a post-processing tool and were tested in steady and unsteady laminar coflow flames [28, 29].

The objective of the present work is to develop a highly-reduced soot model for the prediction of the soot volume fraction, encompassing both the detailed soot precursor chemistry and the physics of particles dynamics interactions. The impact of radiation on both gas and solid phase temperature, which is of primary importance in sooting flames, will be included. For that purpose, we follow a methodology based on a recent approach called *virtual chemistry*, introduced by Cailler *et al.* [30] to predict pollutants formation such as CO [31, 32] or NO<sub>x</sub> [33]. The virtual chemistry method consists in building-up an optimized set of reduced virtual chemical reactions including virtual species. A machine learning algorithm is applied to retrieve a set of user-defined constraints such as the temperature profiles, the heat release or targeted pollutant mass fraction. Here we focus on the prediction of the soot volume fraction. Predictions of the particle number density and the particle size distribution are not be considered in this article.

The virtual chemistry principle is presented in Section 2. In Section 3 an extension of the virtual approach is developed to handle soot formation

in laminar flames. Also, a new procedure is developed in Section 4 to include radiative heat transfer in the computations. The optimization set-up of the virtual models and the computation cases are presented in Section 5. The virtual approach is then validated in 1-D premixed and non-premixed ethylene-air configurations in Section 6. Finally, the virtual chemistry formalism is challenged in a 2-D premixed ethylene-air slot burner and a 2-D non-premixed ethylene-air coflow burner from Santoro *et al.* [34] in Section 7.

## 2. Virtual chemistry basics

The originality of virtual chemistry approach resides in virtual species and reactions whose thermodynamic and chemical properties are optimized using machine learning algorithms in order to retrieve properties of reference flames gathered in a learning database [30]. The virtual reactions between the virtual species do not represent real chemical processes but they form a mathematical architecture designed to reproduce user-specified targets such as temperature and mass fractions of combustion products and pollutant species.

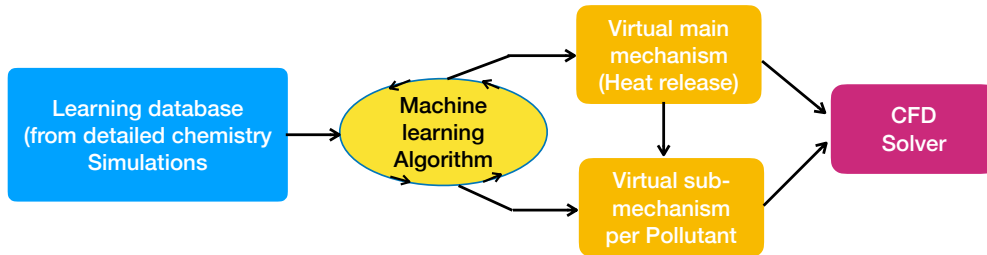


Figure 1: Schematic presentation of virtual chemistry methodology.

A virtual scheme consists of a main block that models the heat release

from the flame and sub-mechanisms dedicated to predict pollutants. Figure 1 depicts a schematic presentation of the approach. Virtual kinetic sub-mechanisms have so far been developed to predict pollutants such as carbon monoxide (CO) [31] and nitrogen oxides (NOx) [33].

The virtual main mechanism structure presented in [30, 31] has shown that the following reaction scheme, composed of 8 virtual species and 2 virtual reactions, accurately captures the heat release and the flame temperature for a wide range of fuel compositions:



In this mechanism,  $F$  represents the fuel,  $Ox$  the oxidizer,  $I$  a virtual intermediate species and  $P_k$  the virtual products.  $\alpha_{k,r}^M$  is the stoichiometric coefficient per unit mass of the  $k^{th}$  virtual species in the  $r^{th}$  virtual reaction, and  $N_P^M$  is the number of virtual products. The superscript  $M$  stands for virtual main chemistry. The vector of reaction parameters  $\chi^M$  (see Supplementary Material) of the main mechanism is optimized through the machine learning algorithm proposed by Cailler *et al.* [30].

Virtual species enthalpy and heat capacity are optimized to recover mixture properties at equilibrium. Unity Lewis number is assumed for the virtual species in the main mechanism.

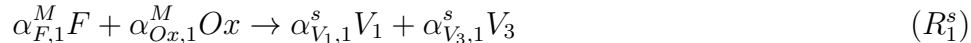
### 3. Virtual soot sub-mechanism

### 3.1. Scheme architecture

As shown in Fig. 2(top), a classical soot model requires first a fine description of the detailed chemistry leading to the soot precursor formation ( $C_2H_2$ , PAHs, etc.) [1]. Then, the formation of the particles is described through a one-precursor ( $C_2H_2$  or PAH) nucleation model [26, 35] or multiple-PAHs approach [1, 36]. Some approaches consider that PAHs grow until they reach an intermediate state, called dimer, between the gas and solid phases [21, 22]. Finally, the solid phase is modeled employing dedicated particles interaction and distribution formalisms such as for instance sectional [8] or MOMs [22] approaches. These successive modeling stages lead to the prediction of the soot characteristics such as volume fraction, particle number density and particle size distribution.

Most of chemical reduction methods, such as tabulated [37] or analytically-reduced [4] approaches, are limited to the gas-phase kinetics. The description of the solid phase, based on classical approaches, remains very time consuming. The virtual soot sub-mechanism proposed in the present work (Fig. 2 bottom) has the advantage of reducing the overall process by targeting the final quantities of interest only.

The soot volume fraction  $f_v^s$  is here targeted. The following chemical structure is proposed to predict the formation of the soot particles species, represented by the virtual chemical species  $\mathcal{S}$ :



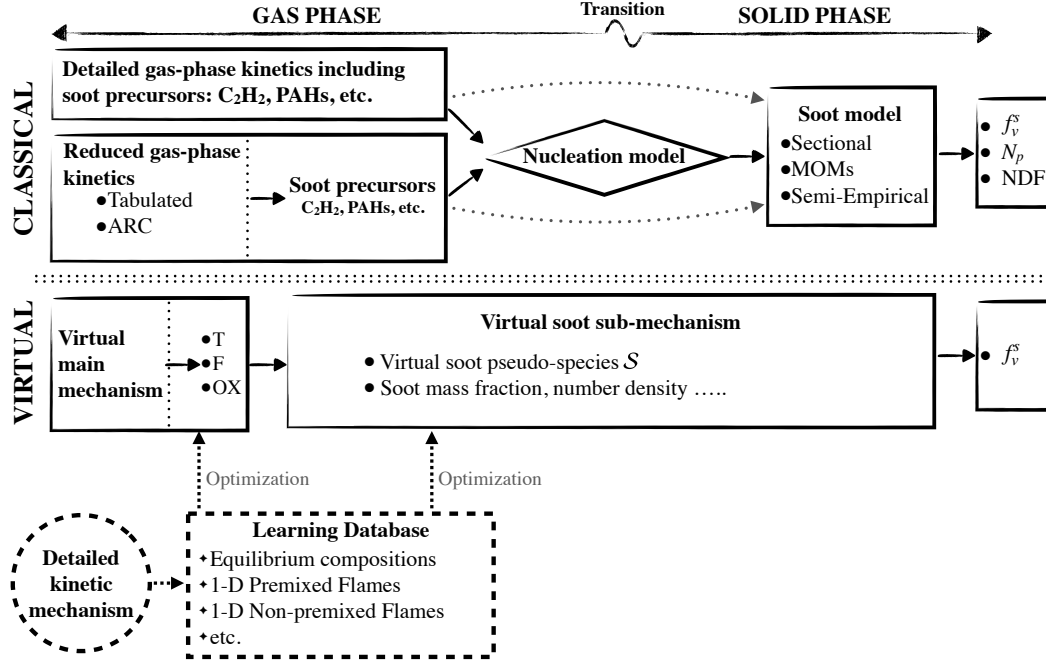


Figure 2: Diagram of soot formation models; top: current soot models, bottom: virtual soot chemistry approach.



where  $V_1$ ,  $V_2$  and  $V_3$  are three virtual species and  $\alpha_{k,r}^s$  is the stoichiometric coefficient per unit mass of the  $k^{th}$  virtual species in the  $r^{th}$  virtual reaction. The superscript  $s$  stands for virtual soot sub-mechanism.

The soot production is initiated by reaction  $R_1^s$ . The rate of progress of this reaction must be equal to that of reaction  $R_1^M$  in order to be consistent

with the fuel oxidation through the main virtual mechanism. The three virtual species  $V_1$ ,  $V_2$  and  $V_3$  together with virtual reactions  $R_2^s$ ,  $R_3^s$  and  $R_4^s$  represent the nucleation, surface growth and coagulation, and oxidation of soot particles. This approach encompasses all the mechanisms of soot formation in both gas and solid phases, without modeling individually each physical step.

### 3.2. Kinetic parameters optimization

The virtual soot sub-mechanism reaction rates of reactions  $R_1^s$  through  $R_4^s$  are expressed as follows:

$$q_1^s = [F]^{n_{F,1}^M} [Ox]^{n_{Ox,1}^M} A_1^M \exp\left(-\frac{E_{a,1}^M}{RT}\right), \quad (1)$$

$$q_2^s = [V_1]^{n_{V_1,2}^s} A_2^s \exp\left(-\frac{E_{a,2}^s}{RT}\right), \quad (2)$$

$$q_3^s = [S]^{n_{S,3}^s} [V_1]^{n_{V_1,3}^s} [V_2]^{n_{V_2,3}^s} A_3^s \exp\left(-\frac{E_{a,3}^s}{RT}\right), \quad (3)$$

$$q_4^s = [S]^{n_{S,4}^s} [Ox]^{n_{Ox,4}^s} [V_2]^{n_{V_2,4}^s} A_4^s T^{\beta_4^s} \exp\left(-\frac{E_{a,4}^s}{RT}\right), \quad (4)$$

where  $E_{a,r}^s$  is the the activation energy,  $A_r^s$  is the pre-exponential constant,  $n_{k,r}^s$  is the order of species  $k$  in reaction  $r$ , and  $\beta_r^s$  is the temperature dependence exponent. As previously mentioned, kinetic rate parameters of Eq. 1 are given by the first reaction  $R_1^M$  of the main mechanism.

The ensemble of virtual chemical parameters of the virtual soot sub-mechanism constitutes a vector  $\chi^s = \{A_r^s, E_{a,r}^s, \alpha_{k,r}^s, n_{k,r}^s, \beta_4^s\}$  to be optimized. It has been observed that the vector  $\chi^s$  depends on the nature of the fuel and of the mixture fraction  $Z$  [31, 33]. Also, the mass conservation imposes:  $\alpha_{V_1,1}^s + \alpha_{V_3,1}^s = 1$ ,  $\alpha_{S,2}^s + \alpha_{V_2,2}^s = 1$  and  $\alpha_{S,3}^s + \alpha_{V_3,3}^s = 3$ .

The kinetic parameters in vector  $\chi^s$  are optimized by minimizing the following cost function:

$$\begin{aligned} C^s(\chi^s) = \sum_{i=1}^{N_c} \left( w_s \frac{\|f_{v,i}^s - f_{v,i}^d\|_{L_2}}{\|f_{v,i}^d\|_{L_2}} \right. \\ \left. + (1 - w_s) \frac{\|\text{grad}f_{v,i}^s - \text{grad}f_{v,i}^d\|_{L_2}}{\|\text{grad}f_{v,i}^d\|_{L_2}} \right), \end{aligned} \quad (5)$$

where  $f_{v,i}^s$  and  $f_{v,i}^d$  are the soot volume fractions of the  $i^{\text{th}}$  flame solution, respectively computed with virtual and detailed reference chemistries and  $\text{grad}f_{v,i}$  indicates the gradient of  $f_{v,i}$ . The superscript  $d$  stands for reference detailed chemistry solutions.  $N_c$  is the number of 1-D reference flame solutions which constitute the learning database. The weight  $w_s$  is set to 0.9, as in the virtual main mechanism [31].

The soot volume fraction  $f_v^s$  is calculated from the virtual soot mass fraction  $Y_S^s$ :

$$f_v^s = \frac{\rho}{\rho_s} Y_S^s \quad (6)$$

where  $\rho$  is the gaseous mixture density, and  $\rho_s$  is the soot density considered constant,  $\rho_s = 1800 \text{ kg m}^{-3}$ .

## 4. Radiative heat transfer modeling

Radiative heat transfer in the gas phase may significantly impact the heat release and the flame temperature. To account for this phenomenon, radiative gas properties of the reactive flow must also be included in the optimization process of the virtual main mechanism. These properties depend on gas temperature and mixture composition [38]. For sooting flames, the Planck mean absorption coefficient  $\kappa_{\text{Planck}}$  can be decomposed as  $\kappa_{\text{Planck}} = \kappa_{\text{gas}} + \kappa_{\text{soot}}$  [39], where  $\kappa_{\text{gas}}$  and  $\kappa_{\text{soot}}$  correspond to gas and solid phases, respectively.

### 4.1. Gas radiation model: virtual approach

The gaseous Planck mean absorption coefficient  $\kappa_{\text{gas}}^M$  is expressed with the polynomial development presented in [38]:

$$\begin{aligned}\kappa_{\text{gas}}^M(Z, T) &= \gamma_0^M(Z) + \gamma_1^M(Z)(1000/T) \\ &+ \gamma_2^M(Z)(1000/T)^2 + \gamma_3^M(Z)(1000/T)^3 \\ &+ \gamma_4^M(Z)(1000/T)^4 + \gamma_5^M(Z)(1000/T)^5,\end{aligned}\tag{7}$$

where the polynomial coefficients  $\gamma_i^M(Z)$  are chosen to retrieve solutions of canonical combustion configurations including radiative heat transfer. The vector of polynomial coefficients  $\Gamma^M = \{\gamma_0^M, \gamma_1^M, \dots, \gamma_5^M\}$  is in practice optimized through the evolutionary algorithm proposed by Cailler *et al.* [30]. The optimization procedure consists in minimizing the following cost function:

$$\mathcal{C}^M(\Gamma^M) = \sum_{i=1}^{N_c} \left( w_M \frac{\|T_i^M - T_i^d\|_{L_2}}{\|T_i^d\|_{L_2}} + (1 - w_M) \frac{|S_{L,i}^M - S_{L,i}^d|}{|S_{L,i}^d|} \right), \quad (8)$$

where  $N_c$  is the number of flame elements included in the learning database, and  $S_{L,i}^d$  and  $T_i^d$  are the targeted reference laminar flame speed and temperature retained for the optimization, respectively. The weight  $w_M$  is set to 0.9, as in Ref. [31].

#### 4.2. Soot particles radiation model

The Planck soot absorption coefficient  $\kappa_{\text{soot}}^v$  is expressed from the soot volume fraction  $f_v^s$  predicted by the virtual soot sub-mechanism and the gas temperature  $T$  given by the main mechanism:

$$\kappa_{\text{soot}}^v = \alpha f_v^s T, \quad (9)$$

where  $\alpha$  is a modeling constant set to  $1302 \text{ m}^{-1}\text{K}^{-1}$  as in Ref. [39].

## 5. Virtual schemes optimization set-up

### 5.1. Learning database and virtual scheme optimization

The reference flame database is generated using the detailed soot kinetics model proposed by the CRECK Modeling Group [1] which consists of 16797 reactions and 297 species. Among these species, 20 lumped pseudo-species called ‘‘BIN’’ are considered. BIN<sub>1</sub> through BIN<sub>4</sub> correspond to heavy PAHs with 20, 40, 80 and 160 carbon atoms respectively. The nascent soot particles are classified as BIN<sub>5</sub> and they grow from spherical shape (BIN<sub>5</sub> to

BIN<sub>12</sub>) until they take an aggregate form (BIN<sub>13</sub> to BIN<sub>20</sub>) [1]. This kinetic mechanism has been extensively validated on several experimental data in many different systems [1, 15, 40]. This mechanism is used here for all detailed chemistry ethylene-air combustion simulations. Radiative heat losses are calculated using the optically-thin narrow-band radiation model based on Ref. [41], which is included in REGATH package [42]. The reference soot volume fraction is defined from the detailed chemistry flame solutions as  $f_v^d = (\rho/\rho_s)Y_{soot}^d$ , where  $Y_{soot}^d = \sum_i Y_{BIN_i}$  for  $i = 5, 6, \dots, 20$  [1].

The virtual main mechanism is trained by employing the genetic algorithm detailed in [31]. The reference flame solutions, used to evaluate the cost function given by Eq. 8, comprise 1-D freely-propagating laminar premixed flames including radiative heat transfer for a range of equivalence ratios covering the flammability limits ( $\phi = 0.5$  and  $\phi = 3.0$ ). It has been shown in [30, 31] that a learning database with similar limits was sufficient to recover heat release and temperature in both premixed and non-premixed flame regimes.

However, to account for multi-mode combustion in the virtual soot sub-mechanism, the learning database is made of both 1-D freely-propagating premixed flames and 1-D counterflow non-premixed flames as in [33]. The database includes 11 1-D premixed flames at atmospheric pressure and initial temperature of 298  $K$  with equivalence ratios from  $\phi = 1.8$  through  $\phi = 2.8$ , by a step of  $\Delta\phi = 0.1$ . It also includes 6 non-premixed counterflow flames, where pure ethylene at 298  $K$  is injected against air at 298  $K$ , covering strain rates from  $a = 6s^{-1}$  to  $a = 95s^{-1}$ , see Table 1. The total number of operating conditions  $N_c$  in the database is  $N_c = N_c^{fpf} + N_c^{cf} = 17$ , with  $N_c^{fpf} = 11$  and

$$N_c^{\text{cf}} = 6.$$

Virtual scheme	Reference archetype	Operating condition
Main mechanism	Adiabatic and Radiative premixed flames	$\phi = \{0.5, \dots, 3.0\}$ ; $\Delta\phi = 0.1$
Soot sub-mechanism	Adiabatic and Radiative premixed and non-premixed flames	$\phi = \{1.8, \dots, 2.8\}$ ; $\Delta\phi = 0.1$ $a = \{6, 10, 25, 45, 60, 95\} \text{ s}^{-1}$

Table 1: List of operating conditions of 1-D flames included in the learning database.

All detailed chemistry simulations include thermophoretic effects for all species BIN<sub>5</sub> to BIN<sub>20</sub>. Unity Lewis number is assumed for virtual species present in the main and virtual mechanisms excepted for the virtual soot species  $\mathcal{S}$  for which  $\text{Le}_{\mathcal{S}} = 25$  is considered. This value is estimated by averaging the Lewis number of BINs found in the detailed mechanism. See the Supplementary Material for more details. All flame calculations, with both detailed and virtual chemistry, are performed using the REGATH package [42].

The optimized reaction rate parameters to account for premixed and non-premixed flames in the virtual soot sub-mechanism are given in the Supplementary Material. The convergence of the cost function  $\mathcal{C}^s(\chi^s)$  defined in Eq. 5 is illustrated in Fig. 3. Here, several realizations of the optimization procedure have been conducted to ensure that the final solution corresponds to a global minimum cost function value as suggested in [31].

### 5.2. Computed cases

The virtual mechanisms and radiation models are now challenged on 1-D and 2-D ethylene-air flames. The following series of computations are performed:

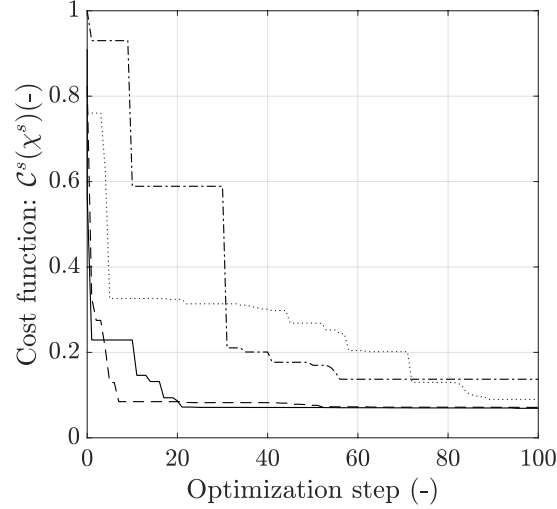


Figure 3: Evolution of the cost function  $\mathcal{C}^s(\chi^s)$  during the optimization process. Each line represents a single realization and the best kinetic parameters set  $\chi^s$  corresponds to the lowest value of the cost function  $\mathcal{C}^s(\chi^s)$  [31].

- D-A: Adiabatic flames using the detailed CRECK mechanism [1];
- D-R: Non-adiabatic flames using the detailed CRECK mechanism [1]. Only gas radiation is considered using the narrow-band radiation model based on Ref. [41] for 1-D configurations, and on that of [38] for 2-D configurations;
- D-Rs: Non-adiabatic flames using the detailed CRECK mechanism [1]. Gas radiation is modeled as in the case D-R, whereas solid phase radiation is modeled using Eq. 9;
- V-A: Adiabatic flames using the developed virtual mechanisms;
- V-R: Non-adiabatic flames using the the virtual mechanism. Only gas radiation is considered;

- V-Rs: Non-adiabatic flames using the the virtual mechanism. Both gas and particle radiation are considered.

Table 2 summarizes the computed cases, indicating the kinetic model and radiative effects involved.

Computed case	D-A	D-R	D-Rs	V-A	V-R	V-Rs
Kinetic model	Detailed mechanism			Virtual mechanism		
Adiabatic	✓	–	–	✓	–	–
Gas radiation	–	✓	✓	–	✓	✓
Soot radiation	–	–	✓	–	–	✓

Table 2: Summary of computed cases. Kinetic model and radiative effects involved are indicated.

## 6. 1-D laminar ethylene-air flame computations

### 6.1. Validation of virtual main mechanism

#### 6.1.1. 1-D freely-propagating premixed flames

Simulations of 1-D freely-propagating premixed ethylene-air flames are first conducted. The laminar consumption speed  $S_L$  is plotted in Fig. 4 as a function of the equivalence ratio  $\phi$ . The virtual approach predicts very well the flame speed in all conditions. As the radiative heat losses take place essentially in hot gases, the flame front and the flame speed  $S_L$  are not affected by radiation.

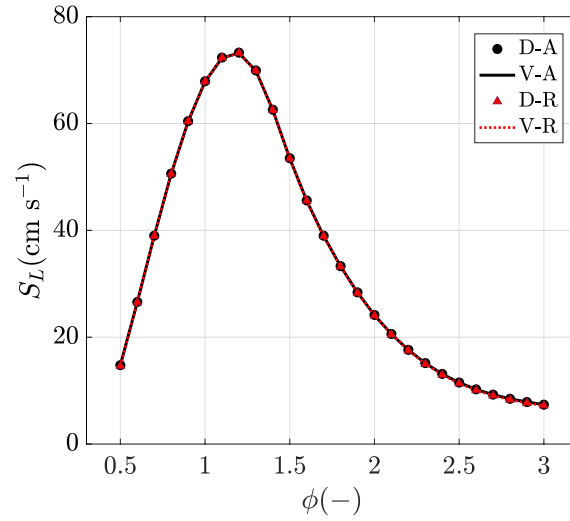


Figure 4: Evolution of the laminar flame speed of 1-D premixed ethylene-air flames ( $P = 1$  atm,  $T_0 = 298$  K): comparison between the four cases D-A, D-R, V-A, V-R.

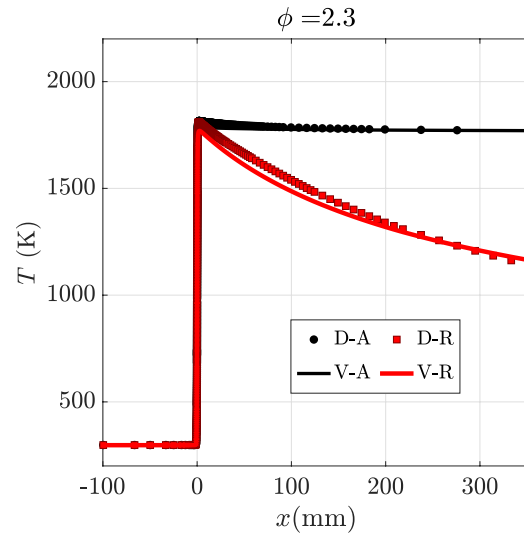


Figure 5: Impact of radiative heat losses on temperature profile in a 1-D freely-propagating premixed ethylene-air flame ( $\phi = 2.3$ ): comparison between the four cases D-A, D-R, V-A, V-R.

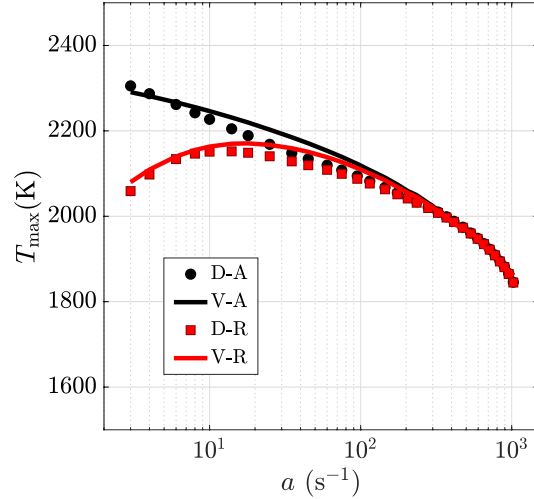


Figure 6: Evolution of the maximum temperature  $T_{\max}$  with the strain rate  $a$  in 1-D non-premixed ethylene-air counterflow flames: comparison between the four cases D-A, D-R, V-A, V-R.

Figure 5 presents temperature profiles obtained at  $\phi = 2.3$  for four cases D-A, D-R, V-A, and V-R. Both the adiabatic and non-adiabatic virtual mechanisms reproduce very well the reference temperature profiles. The impact of radiation on the temperature, especially visible for long distances (long residence times), is well captured by the virtual chemistry and radiation models.

### 6.1.2. 1-D non-premixed counterflow flames

The gas phase virtual radiative model is validated in this section for non-premixed flames. Four series of 1-D ethylene-air counterflow flames are computed at different strain rates  $a$  again for the four conditions D-A, D-R, V-A, and V-R. Figure 6 illustrates the evolution of the maximum flame temperature with the strain rate. In both adiabatic and radiative cases,

the virtual main chemistry and virtual radiative models predict very well this evolution for a very wide range of strain rates, from equilibrium up to quenching conditions. As expected, radiative heat losses affect the maximum flame temperature at very low strain rates.

## 6.2. Validation of soot virtual sub-mechanism and virtual radiative model

### 6.2.1. 1-D freely-propagating premixed flames

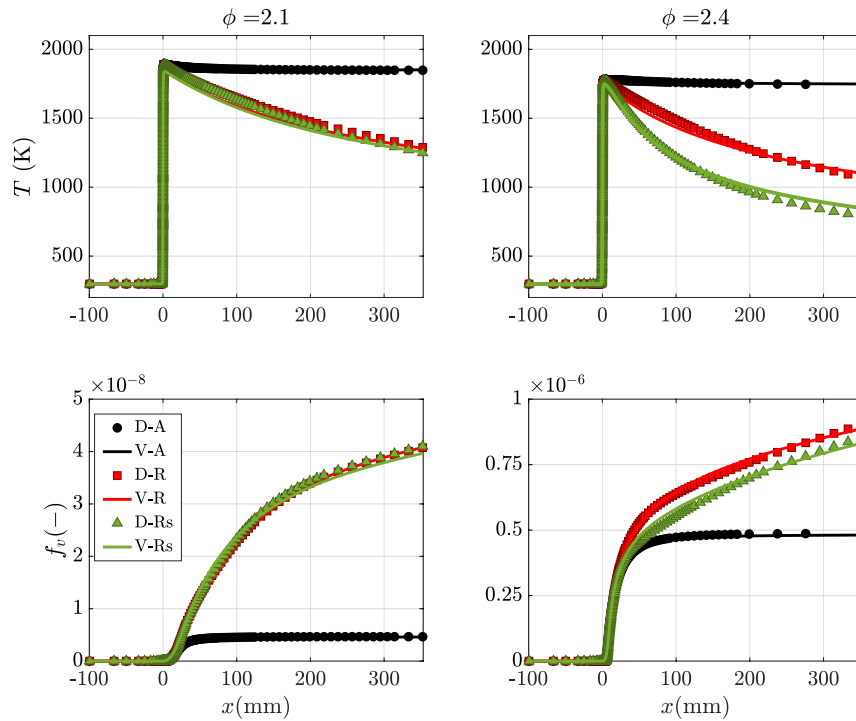


Figure 7: Temperature (top) and soot volume fraction (bottom) profiles of premixed ethylene-air flames, with and without considering solid particle radiation for different equivalence ratios  $\phi = 2.1$  (left) and  $\phi = 2.4$  (right): comparison between the six cases: D-A, D-R, D-Rs, V-A, V-R, V-Rs.

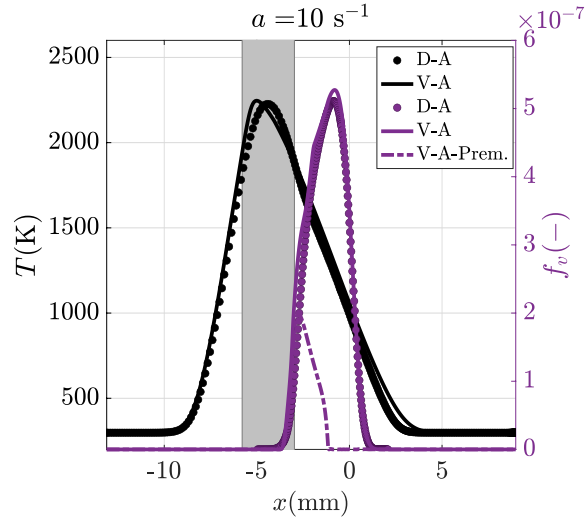


Figure 8: Temperature and soot volume fraction profiles of adiabatic and non-adiabatic 1-D non-premixed counterflow flame using detailed and virtual models, cases D-A and V-A. Soot volume fraction profile obtained by a virtual soot sub-mechanism optimized on a learning database including only 1-D premixed flames (V-A-Prem.) is also plotted. The region covered by the learning database of only 1-D premixed flames within the extinction limits is shown by the grey area.

Temperature and soot volume fraction profiles are shown in Fig. 7 for equivalence ratios equal to 2.1 and 2.4, respectively. Solutions are plotted for the six simulation cases D-A, D-R, D-Rs, V-A, V-R and V-Rs.

Again, for both  $\phi = 2.1$  and  $\phi = 2.4$ , comparisons between D-A/V-A and D-R/V-R results in Fig. 7 (top) show that the virtual main mechanism accurately captures the temperature profiles with and without considering gas radiation. The soot volume fraction profiles, plotted in Fig. 7 (bottom) are also very well predicted by the virtual soot sub-mechanism for these operating conditions. The soot production, enhanced by radiative heat transfer, also significantly increases by more than 2 orders of magnitude between  $\phi = 2.1$

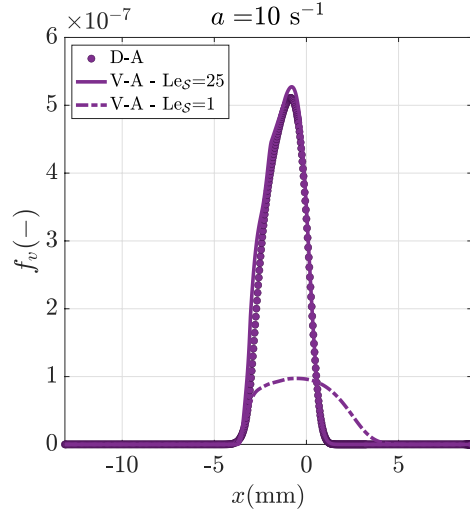


Figure 9: Influence of the virtual soot species  $\mathcal{S}$  Lewis number,  $Le_{\mathcal{S}}$ , on soot volume fraction in a counterflow ethylene-air flame.

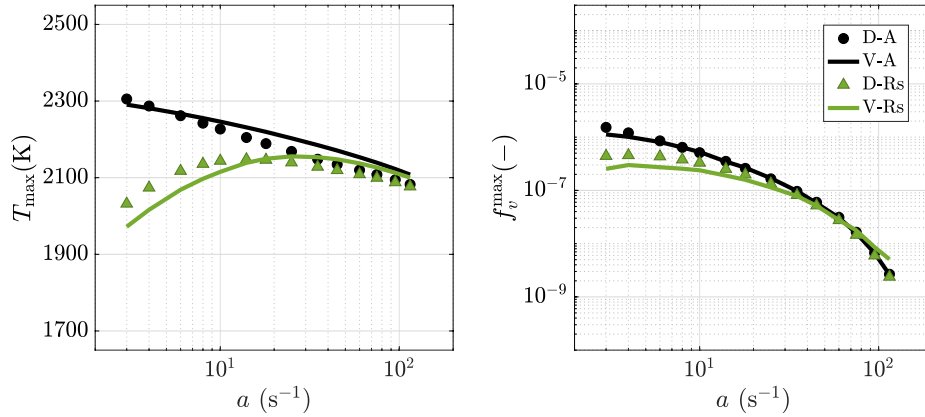


Figure 10: Evolution of the maximum temperature  $T^{\max}$  (left), and maximum soot volume fraction  $f_v^{\max}$  (right) as a function of strain rate  $a$  in 1-D counterflow non-premixed ethylene-air flames: comparison between for the four cases D-A, V-A, D-Rs, and V-Rs.

and  $\phi = 2.4$ .

The influence of solid phase radiation on temperature is only significant

for  $\phi = 2.4$ , where the soot volume fraction is high enough (cases D-Rs and V-Rs). The virtual model which includes both gas and solid particles radiation predicts very well the temperature and soot reference solutions.

### 6.2.2. 1-D non-premixed counterflow flames

Figure 8 presents temperature and soot volume fraction profiles for an adiabatic 1-D non-premixed counterflow flame (strain rate  $a = 10 \text{ s}^{-1}$ ) computed with both detailed (D-A) and virtual (V-A) chemistry approaches. Pure ethylene is injected from right while air is injected from left. Soot formation takes place in a rich region located between the maximal flame temperature position ( $x = -4\text{mm}$ ) and the stagnation plane ( $x = 0$ ). The soot volume fraction is well predicted by the virtual soot sub-model trained to capture both premixed and non premixed flame archetypes as indicated on Table 1.

It is interesting to focus on the dashed-dotted profile that shows the soot volume fraction profile obtained with a virtual scheme sub-mechanism (V-A-Prem.) trained to target only 1-D premixed flames. The target premixed flames are accessible only within the flammability limits, highlighted by the grey area in Fig 8. The peak of the soot volume fraction is located at the rich side of the grey zone. It can be seen that such target flame is unable to capture the soot produced here above the rich extinction limit.

As indicated in Sec. 5.1, the virtual scheme used in case V-A has been optimized with a Lewis number of species  $\mathcal{S}$  set to  $Le_{\mathcal{S}} = 25$  whereas  $Le=1$  has been assumed for all other virtual species (see the Supplementary Material for the choice of  $Le_{\mathcal{S}} = 25$ ). As soot particles diffusion is very small compared to gaseous species, assuming unity Lewis also for the soot would have been

unrealistic. This is illustrated in Fig. 9 where the solution obtained with  $Le=1$  for all species considerably underestimates the soot production.

Finally, the evolution of maximum temperature  $T^{\max}$  and maximum soot volume fraction  $f_v^{\max}$  as a function of strain rate  $a$  are presented in Fig. 10 for adiabatic simulation cases D-A and V-A as well as non-adiabatic cases D-Rs and V-Rs including both gaseous and solid phases radiative heat losses. The virtual soot sub-mechanism predicts well the soot volume fraction maximum value  $f_v^{\max}$  of 1-D counterflow ethylene-air flames for a large range of strain rates  $a$ .

### 6.3. Application of virtual models to burner-stabilized flames

The reduced chemistry approach is now applied to a burner-stabilized ethylene-air flame studied within the International Sooting Flame (ISF) Workshop [45]. Two equivalence ratio of  $\phi = 2.34$  and  $\phi = 2.64$  are investigated at atmospheric pressure and temperature of  $T = 298$  K. Simulations are conducted by imposing at the inlet the fresh gases injection velocity measured in experiments [43, 44] ( $6.73 \text{ cm}\cdot\text{s}^{-1}$ ). Figure 11 (top) show that for both detailed and virtual radiative simulations, numerical prediction of temperature agrees very well with experimental measurements [43]. Soot volume fraction profiles plotted in Fig. 11 (bottom), exhibit also a fair agreement between simulations and experimental data. Therefore, even if burner-stabilized flames were not included in the learning database, the virtual chemistry is able to capture their chemical structure.

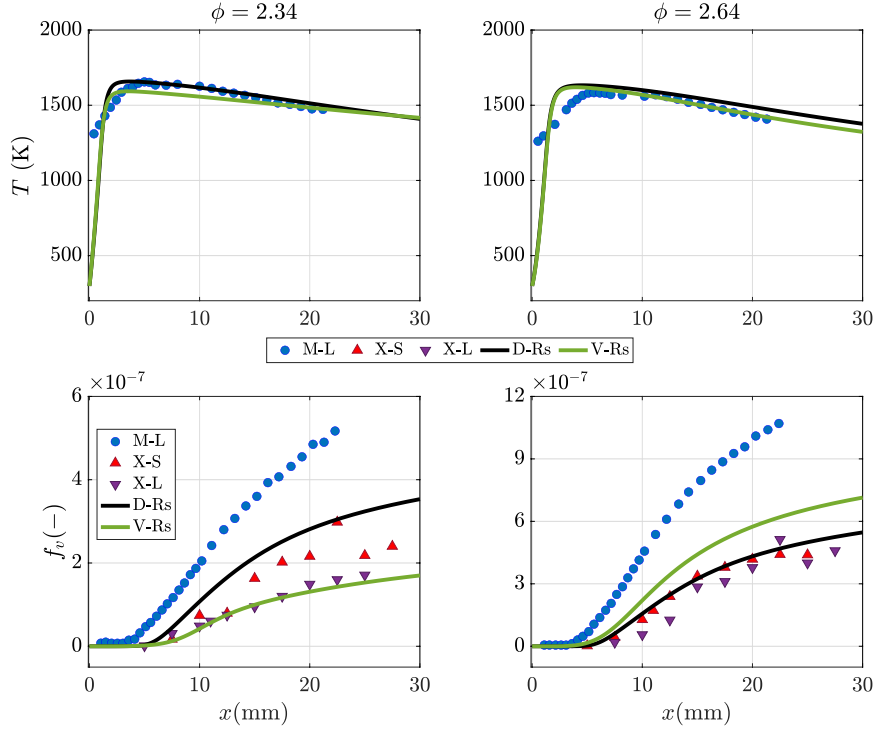


Figure 11: Burner-stabilized premixed ethylene-air flames for  $\phi = 2.34$  and  $\phi = 2.64$ . Comparison of numerical results (D-Rs and V-Rs) of temperature (top) and soot volume fraction (bottom) profiles against experiments; (M-L) Menon et al. [43] and (X-S, X-L) Xu et al. [44].

## 7. Application of virtual models to 2-D laminar flames

In this section, the three simulation cases V-A, V-R and V-Rs (see Table 2) are challenged in two two-dimensional laminar flame configurations. First, a 2-D premixed ethylene-air slot burner is simulated. Next, the non-premixed Santoro coflow burner [34] from ISF workshop is studied.

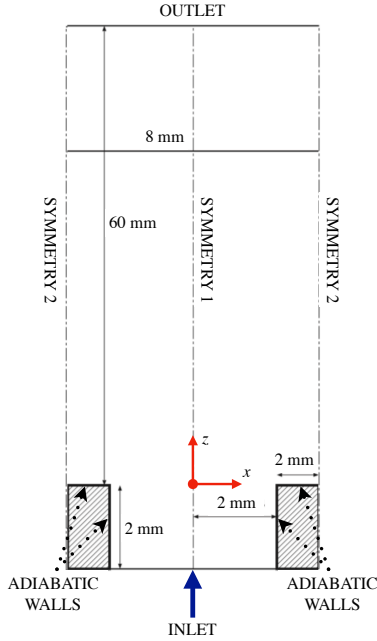


Figure 12: Premixed slot burner: geometry of the numerical setup used in simulations.

### 7.1. 2-D laminar ethylene-air premixed slot burner

The geometry of the premixed slot burner is shown in Fig. 12. The domain is long enough to allow soot formation. The cell size in the flame front are  $\Delta_x \sim 0.03$  mm, leading to 15-20 cells across the thermal layer.

Boundary conditions are indicated in Fig. 12. The burner walls are adiabatic. The computation is carried out on half of the domain because of the symmetric geometry of the burner. Symmetry is also assumed for outer lateral boundary conditions. Ethylene-air mixture with equivalence ratio of  $\phi = 2.5$  at  $T = 298$  K and  $p = 1$  atm is injected at the inlet. A parabolic axial velocity distribution, with mean axial velocity  $u_m = 30$  cm  $\cdot$  s $^{-1}$ , is imposed to mimic a fully-developed channel flow. The six numerical cases presented in Sec. 5.2 are computed. Simulations are carried out with the laminarSMOKE

package [46, 47] based on the OpenFOAM framework, designed to handle arbitrarily complex kinetic mechanisms.

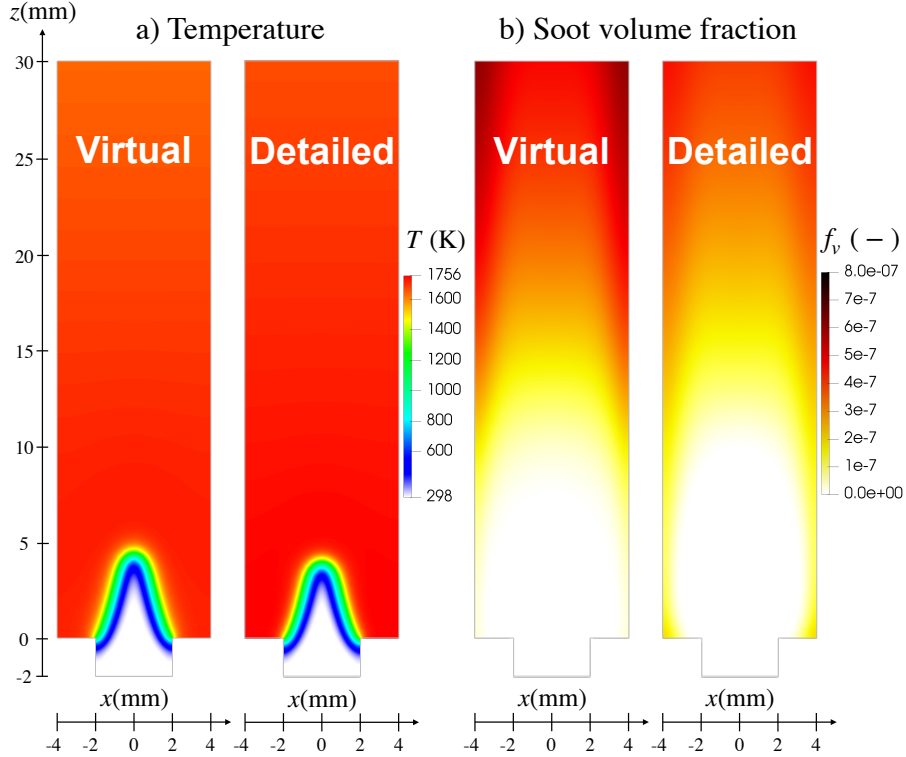


Figure 13: Premixed Slot Burner: comparison of a) temperature and b) soot volume fraction fields using the virtual and detailed models, case V-R (left) and case D-R (right).

Figure 13 compares the virtual soot sub-mechanism (case V-R) and the detailed model (case D-R) results. The analysis of predicted temperature fields shows the ability of the virtual chemistry to capture accurately the flame position. Flame heights of 6 mm and 6.3 mm are found respectively for D-R and V-R cases (5 % error). A good agreement is also observed on the soot volume fraction fields. Temperature and soot volume fraction profiles along the centerline are plotted in Fig. 14 for the six simulation cases D-A,

D-R, D-Rs, V-A, V-R and V-Rs. All temperature profiles show very good agreement with the detailed chemistry simulations. The temperature in all cases differs in about 2 to 3%. Heat losses are fairly captured by the virtual radiation model. The soot volume fraction profiles are also well predicted by the three approaches. The maximum soot volume fraction in case (c) presents an error of about 15 %, which is the maximum between the three cases. When radiative effects are included, earlier soot inception is observed as in 1-D flames results.

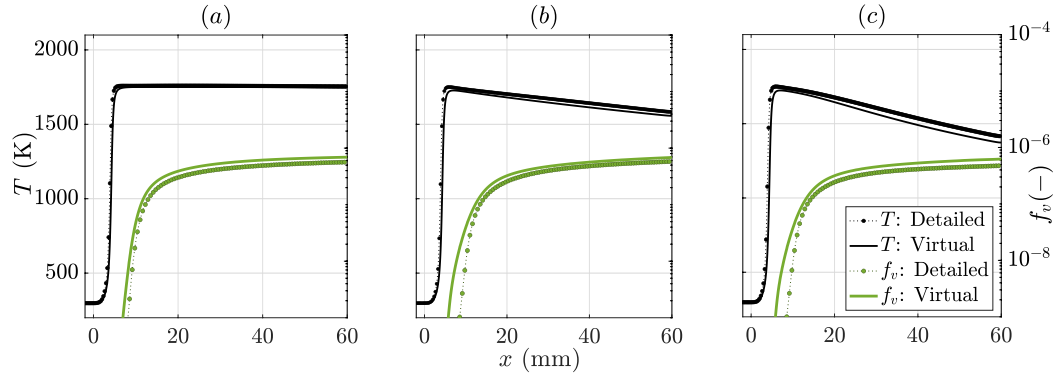


Figure 14: Premixed Slot Burner: Temperature (black) and soot volume fraction (green) profiles along the centerline. Comparison of simulation (a) between cases D-A and V-A, (b) between cases D-R and V-R, and (c) between cases D-Rs and V-Rs.

Figure 15 displays the radial temperature profiles for the six simulation cases at two different heights above the burner  $z = 3$  mm and  $z = 20$  mm. At  $z = 3$  mm, the difference of the flame thickness is about 0.1 mm between detailed (D-A, D-R, D-Rs) and virtual (V-A, V-R, V-Rs) results. Further downstream at  $z = 20$  mm, the temperature profile is almost uniform and exhibits a difference of less than 2% between detailed and reduced simulations.

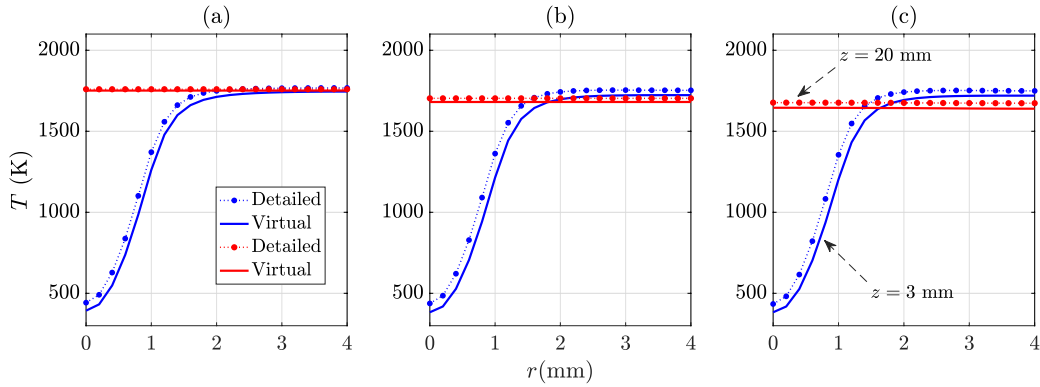


Figure 15: Premixed Slot Burner: radial temperature profiles at two different heights above the burner,  $z = 3$  mm (blue) and  $z = 20$  mm (red). Comparisons (a) between cases D-A and V-A, (b) between cases D-R and V-R, and (c) between cases D-Rs and V-Rs.

Figure 16 displays the radial soot volume fraction profiles for the six different cases at  $z = 3$  mm and  $z = 20$  mm. At  $z = 3$  mm, the virtual adiabatic model (a) underestimates the peak of soot volume fraction given by the reference solution by two orders of magnitude. The discrepancies are reduced to a factor of two when radiative effects are included. At  $z = 20$  mm, the mismatch is even limited to 25 % for the three cases.

Table 3 presents a comparison of the computational cost required by virtual and detailed chemistries to simulate the premixed slot burner. A speed-up of more than 2000 is observed when using the virtual scheme.

## 7.2. 2-D laminar Santoro Coflow Burner

The non-premixed flame experimentally studied by Santoro *et al.* [34] is now computed with the virtual soot model. The burner consists of a central pipe fed with pure ethylene surrounded by a concentric tube for air injection. The fuel and air flow rates are  $3.85 \text{ cm}^3 \cdot \text{s}^{-1}$  and  $713.3 \text{ cm}^3 \cdot \text{s}^{-1}$ , respectively.

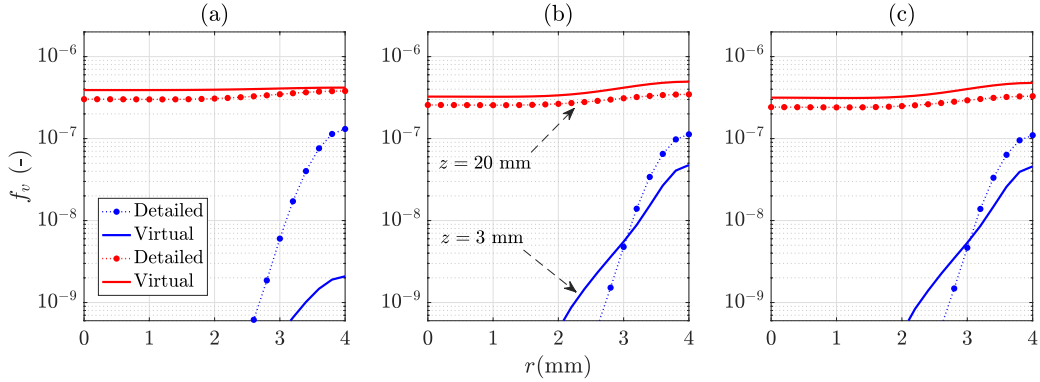


Figure 16: Premixed Slot Burner: radial soot volume fraction profiles at two different heights above the burner,  $z = 3$  mm (blue) and  $z = 20$  mm (red). Comparisons (a) between cases D-A and V-A, (b) between cases D-R and V-R, and (c) between cases D-Rs and V-Rs.

Physical time	Computational time using Virtual Chemistry	Computational time using Detailed chemistry	Speed-up
1 ms	30 s	17.5 h	2100
50 ms	25 min	850 h	2040

Table 3: Comparison of the CPU time (per core) with the virtual scheme (12 species, 6 reactions) and the detailed CRECK scheme [1] (297 species and 16797 reactions) . The numerical cost has been estimated by computing the 2-D premixed slot burner on 120 cores (Intel Xeon CPU E5-2670), without accounting for radiation.

Further details on the experimental setup are given in [34].

The 2-D numerical domain is 152 mm long and 47.5 mm wide. Following ISF recommendations [45], symmetry condition is retained at the centerline and slip walls are prescribed for the outer lateral boundary. The cartesian grid is made of 26270 cells with a characteristic size of  $\Delta_x \sim 0.075$  mm in the flame region, close to values used in [48]. The inlet fuel velocity follows a

parabolic distribution adapted to fully-developed flow with a mean velocity  $u_m^{\text{fuel}} = 3.98 \text{ cm} \cdot \text{s}^{-1}$ . Constant velocity  $u_m^{\text{coflow}} = 8.9 \text{ cm} \cdot \text{s}^{-1}$  is prescribed at the air inlet. Both fuel and air are injected at  $T = 298 \text{ K}$ . The inner tube wall temperature is imposed at  $T = 350 \text{ K}$ . Simulations are carried out with the laminarSMOKE package [46, 47] based on the OpenFOAM framework.

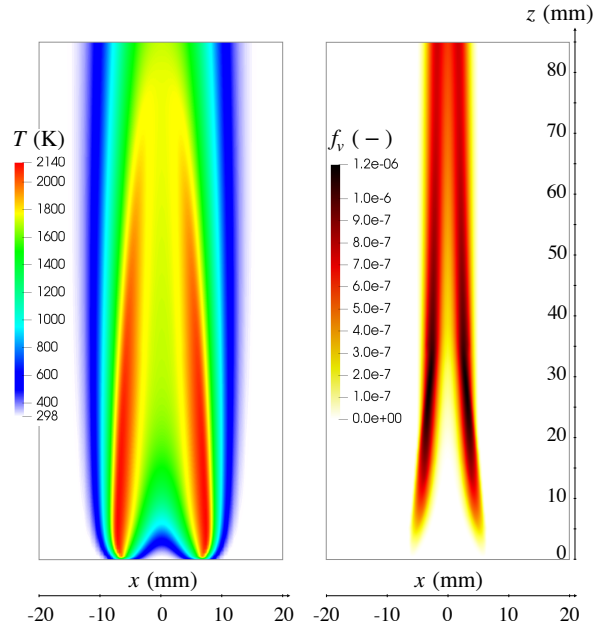


Figure 17: Santoro Coflow Flame: Temperature (left) and soot volume fraction (right) fields using the virtual chemistry and radiative models.

The virtual chemistry simulation includes both gas and solid phases radiation phenomena (V-Rs), which are both significant in this configuration [49]. 2-D iso-contour of temperature and soot volume fraction fields are shown in Fig. 17.

Radial profiles of temperature are plotted in Fig. 18 (a) for two heights above the burner at  $z = 10 \text{ mm}$  and  $50 \text{ mm}$ . Numerical results using the

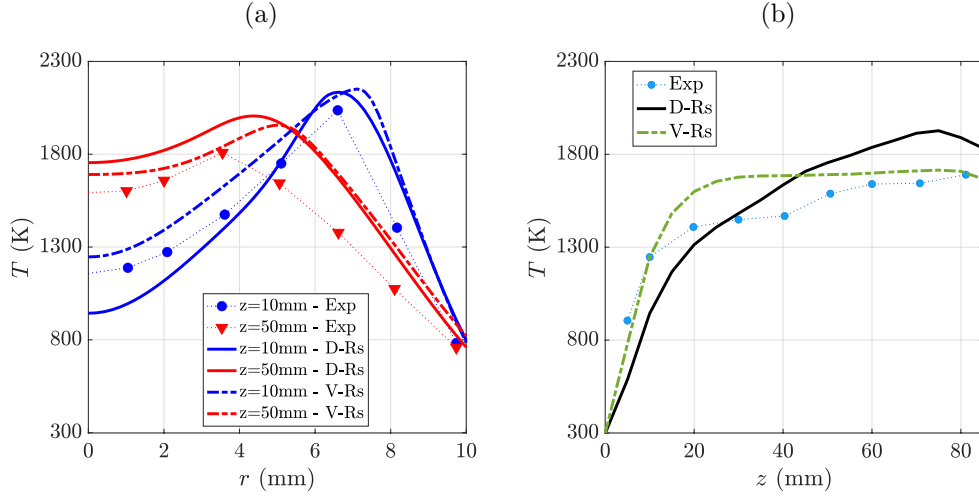


Figure 18: Santoro Coflow Flame: Temperature profiles; (a) radial, and (b) axial. Comparison between detailed (D-Rs), solid lines, and virtual chemistry (V-Rs), dashed lines.

virtual non-adiabatic models (V-Rs) are in good agreement with detailed simulation (D-Rs) results and experimental data from [49]. The relative errors for the maximum temperature between numerical results and experimental data are about 5 % at  $z = 10$  mm and 10 % at  $z = 50$  mm. Both numerical models overestimate the flame thickness. The temperature peak positions are shifted by about 1.5 mm at  $z = 10$  mm and about 0.5 mm at  $z = 50$  mm.

The centerline temperature profiles, plotted in Fig. 18 (b), show an overprediction of 15 % by the virtual model (V-Rs) in the interval  $15 < z < 45$  mm, while the detailed chemistry model (D-Rs) underpredicts for  $z < 30$  mm and overpredicts for  $z > 30$  mm.

Radial profiles of soot volume fraction are presented in Fig. 19 (a), at  $z = 10$  mm and  $z = 50$  mm, downstream the burner exit. The virtual model (V-Rs) fairly reproduces the soot volume fraction profiles compared

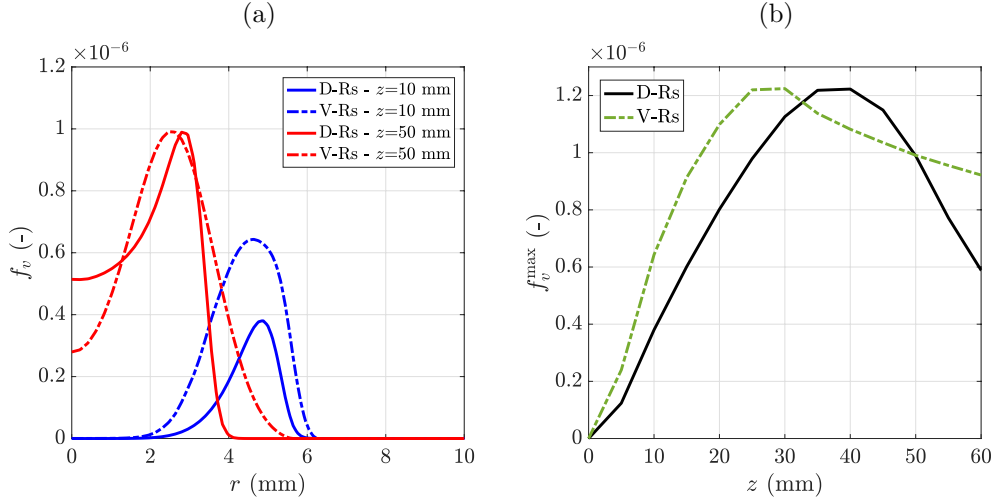


Figure 19: Santoro Coflow Flame: (a) Soot volume fraction radial profiles at two different heights above the burner,  $z = 10$  mm (blue) and  $z = 50$  mm (red), (b) Axial evolution of the maximum soot volume fraction in the radial direction. Comparison between detailed (D-Rs), solid lines, and virtual chemistry (V-Rs), dashed lines.

to detailed reference results (D-Rs) at both heights. At  $z = 10$  mm, the difference in the maximum soot volume fraction is about 40 %. Figure 19 (b) shows the axial evolution of the maximum soot volume fraction in the radial direction. The virtual approach (V-Rs) reproduces the maximum value of  $f_v$  as in the detailed simulations (D-Rs), but with a peak position 10 mm closer to the burner exit. Soot is not well oxidized at the flame tip when using the virtual model (V-Rs), where the difference of maximum soot volume fraction compared to the detailed model results (D-Rs) is about 50 % at  $z = 60$  mm.

Axial profiles of radially-integrated soot volume fraction, defined as  $F_v(z) = \int_r 2\pi f_v(r, z) r dr$ , are shown in Fig 20. In addition to D-Rs solutions, detailed chemistry solutions obtained by other groups are also indicated. Simulation

results of Blacha *et al.* [18] have been obtained using a detailed chemistry mechanism including 71 species and 803 reactions. Soot particles distribution has been modeled with a sectional method whereas radiative heat transfer from gas and soot particles are captured with the assumption of an optically thin medium according to Di Domenico *et al.* [50]. Simulation results of Akridis and Rigopoulos [51] have been obtained using a detailed mechanism including 75 species and 529 reactions [52]. A discretized population balance equation for soot the particles is solved, where its source terms closures are based on different models from the literature [53–55]. An optically thin approximation for the radiation of gas species ( $\text{H}_2\text{O}$ ,  $\text{CO}_2$  and  $\text{CO}$ ) and soot particles from Kronenburg *et al.* [56] is here considered. Finally, experimental measurements from ISF database [45] are also added in this figure (blue circles).

These results highlight qualitative differences between the three detailed soot formation mechanisms solutions. Soot volume fraction tendency predicted by the virtual soot sub-mechanism is consistent with the three complex chemistry solutions and with the experimental data: soot particles are produced in the first half of the domain before being consumed downstream. Deepening the analysis of the differences between the virtual chemistry solutions and experimental data is not relevant here, as the accuracy of the reduced model is naturally limited to that of the reference detailed mechanism retained (CRECK) to generate the learning database.

In comparison with the CRECK detailed mechanism (D-Rs), the rate of soot oxidation process downstream the burner is underestimated by the virtual scheme (V-Rs). We attribute this drawback to the flame archetypes

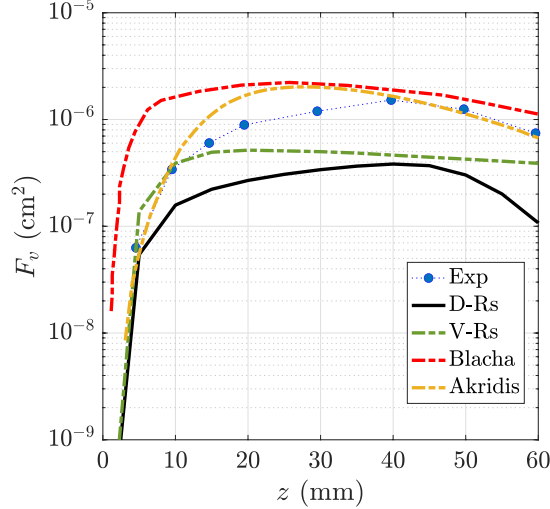


Figure 20: Santoro Coflow Flame: Integrated soot volume fraction profiles along the centerline. Comparison of detailed and virtual chemistry results against experimental measurements. Numerical results from other groups are also included.

retained in the learning database. Indeed, close to the fuel injection, the chemical flame structure follows a classical non-premixed flame where pure fuel diffuses into pure air. Such flame archetype has been well targeted during the optimization process. However, further downstream, burnt gases mix with surrounding air coflow before entering the soot chemistry reactive region. In this case, the flame archetype is therefore closer to a diluted air/burnt gases stream, a configuration which has not been considered in the learning database during the virtual soot sub-mechanism optimization process.

To further pursue these analyses, the learning database used to train the virtual scheme, which includes premixed and non-premixed flames is projected in subspaces  $(T, Z)$  and  $(f_v, Z)$  in Figs. 21 (a) and (b), respectively.

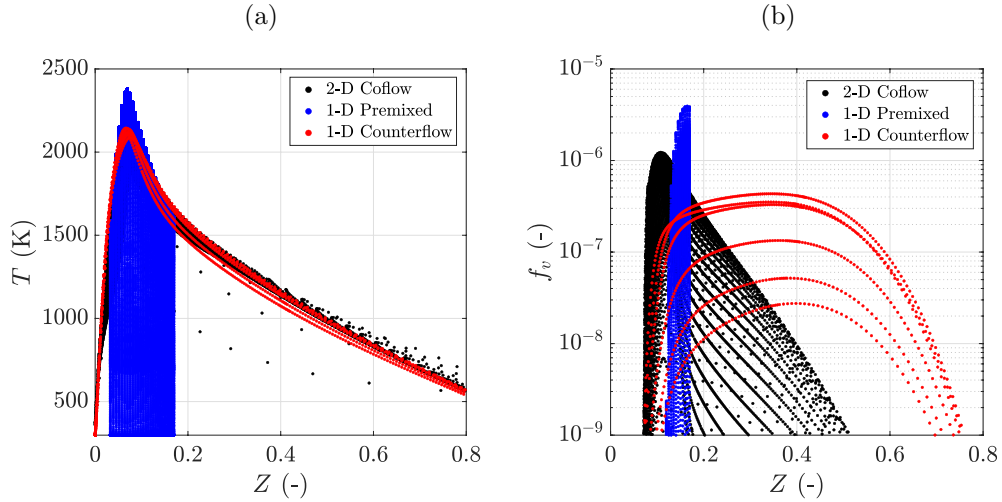


Figure 21: Scatter plot in the (a)  $(T, Z)$  and (b)  $(f_v, Z)$  phase spaces using the reference detailed mechanism results: points of 1-D premixed (blue) and non-premixed counterflow (red) flames as well as results from the 2-D coflow flame (black) simulation from Section 7.2 are presented.

The chemical trajectories effectively followed by the 2-D Santoro computation are superimposed to these subspaces. Most of the chemical trajectories are in practice well covered by the learning database in the  $(T, Z)$  subspace. However, the projection of the Santoro flame solution in the  $(f_v, Z)$  subspace reveals some incompleteness of the training database. Indeed, for  $Z$  between 0.063 and 0.12 (equivalence ratios between 1 and 2 respectively), several trajectories exceed by an order of magnitude the upper envelopes given by premixed and non-premixed flame solutions. Complementary flame archetypes should then be targeted during the optimization step to entirely capture the soot formation process.

## 8. Conclusions and discussion

A new reduced virtual chemistry model is developed to predict the temperature profiles, heat release rate and soot volume fraction in laminar ethylene-air flames. Also, a virtual approach is proposed in order to include gas phase radiative heat transfer in the simulations. This new virtual approach integrates for the first time both gaseous and solid phases in a virtual mechanism, by bypassing the gas-solid complex formalism without explicit mathematical distinction between both phases.

Numerical results using the new virtual model are validated in 1-D ethylene air flames in canonical configurations, such as premixed and non-premixed flames, against reference detailed chemistry calculations. Additionally, the virtual model is challenged in a 1-D burner-stabilized flame configuration, giving very good results when compared to reference detailed chemistry calculations and experimental measurements. This shows that the virtual model is capable to predict soot formation in configurations other than those used to build the reference database.

Furthermore, simulations in two 2-D configurations are carried out using the virtual models: a premixed slot burner and a non-premixed coflow burner from the ISF workshop. In both configurations, very good results of the flame structure and soot characteristics are obtained. Also, the new virtual radiative model well provides the heat losses. In overall, the new virtual soot sub-mechanism captures soot physical phenomena with good level of accuracy and is comparable to other numerical works in the literature with more detailed models. By adding representative flames in the reference database used for the generation of the virtual model, one would be able to cover both

smoking and non-smoking conditions in Santoro’s flame [34, 49, 57].

In general, a massive reduction of the soot kinetics model is obtained, passing from 297 species and 16797 reactions in the reference detailed mechanism to 12 virtual species and 6 virtual reactions in the virtual mechanism, without need of additional models for solid particles. This chemical reduction has a big impact on the computational time of the simulations. When using the virtual model in 2-D laminar flames simulations, the CPU cost is reduced by a factor of about 2100 compared detailed models.

Perspectives to this work are to apply the soot virtual scheme to turbulent flames encountered in practical applications. The main difficulty would be to handle the different chemical paths followed by the various flame elements encountered in turbulent reactive flows. By training the virtual scheme on both premixed and non-premixed strained flamelets, it is expected to accurately capture most local combustion elements encountered in practical turbulent flames. If this is not sufficient, additional flame configurations may be added to the training database.

## **Acknowledgments**

This work was granted access to the HPC resources of TGCC under the allocations A0092B10253 made available by GENCI (French Grand Equipement National de Calcul Intensif), and HPC resources from the Mésocentre computing center of CentraleSupélec and Ecole Normale Supérieure Paris-Saclay supported by CNRS and Région Ile-de-France (<http://mesocentre.centralesupelec.fr/>).

## References

- [1] C. Saggese, S. Ferrario, J. Camacho, A. Cuoci, A. Frassoldati, E. Ranzi, H. Wang, T. Faravelli, Kinetic modeling of particle size distribution of soot in a premixed burner-stabilized stagnation ethylene flame, *Combust. Flame* 162 (2015) 3356–3369.
- [2] B. Fiorina, R. Mercier, G. Kuenne, A. Ketelheun, A. Avdić, J. Janicka, D. Geyer, A. Dreizler, E. Alenius, C. Duwig, et al., Challenging modeling strategies for LES of non-adiabatic turbulent stratified combustion, *Combust. Flame* 162 (2015) 4264–4282.
- [3] B. Fiorina, Accounting for complex chemistry in the simulations of future turbulent combustion systems, in: *AIAA Scitech 2019 Forum*, 2019, p. 0995.
- [4] P. Pepiot, Automatic strategies to model transportation fuel surrogates, Ph.D. thesis, Stanford University, 2008.
- [5] A. Felden, E. Riber, B. Cuenot, Impact of direct integration of analytically reduced chemistry in LES of a sooting swirled non-premixed combustor, *Combust. Flame* 191 (2018) 270–286.
- [6] L. Gallen, A. Felden, E. Riber, B. Cuenot, Lagrangian tracking of soot particles in LES of gas turbines, *Proc. Combust. Inst.* 37 (2019) 5429 – 5436.
- [7] M. E. Mueller, H. Pitsch, LES model for sooting turbulent nonpremixed flames, *Combust. Flame* 159 (2012) 2166 – 2180.

- [8] P. Rodrigues, B. Franzelli, R. Vicquelin, O. Gicquel, N. Darabiha, Coupling an LES approach and a soot sectional model for the study of sooting turbulent non-premixed flames, *Combust. Flame* 190 (2018) 477 – 499.
- [9] B. Fiorina, D. Veynante, S. Candel, Modeling combustion chemistry in large eddy simulation of turbulent flames, *Flow Turbul. Combust.* 94 (2015) 3–42.
- [10] R. Said, A. Garo, R. Borghi, Soot formation modeling for turbulent flames, *Combust. Flame* 108 (1997) 71–86.
- [11] W. Kollmann, I. M. Kennedy, M. Metternich, J.-Y. Chen, Application of a soot model to a turbulent ethylene diffusion flame, in: *Soot Formation in Combustion*, Springer, 1994, pp. 503–526.
- [12] B. Franzelli, E. Riber, B. Cuenot, M. Ihme, Numerical modeling of soot production in aero-engine combustors using large eddy simulations, *ASME Turbo Expo 2015* (2015).
- [13] M. Celnik, R. Patterson, M. Kraft, W. Wagner, Coupling a stochastic soot population balance to gas-phase chemistry using operator splitting, *Combust. Flame* 148 (2007) 158 – 176.
- [14] C. J. Pope, J. B. Howard, Simultaneous particle and molecule modeling (spamm): An approach for combining sectional aerosol equations and elementary gas-phase reactions, *Aerosol Sci. Technol.* 27 (1997) 73–94.
- [15] W. Pejpichestakul, E. Ranzi, M. Pelucchi, A. Frassoldati, A. Cuoci, A. Parente, T. Faravelli, Examination of a soot model in premixed

- laminar flames at fuel-rich conditions, *Proc. Combust. Inst.* 37 (2019) 1013 – 1021.
- [16] M. D. Smooke, C. S. McEnally, L. D. Pfefferle, R. J. Hall, M. B. Colket, Computational and experimental study of soot formation in a coflow, laminar diffusion flame, *Combust. Flame* 117 (1999) 117–139.
- [17] Q. Zhang, M. Thomson, H. Guo, F. Liu, G. Smallwood, A numerical study of soot aggregate formation in a laminar coflow diffusion flame, *Combust. Flame* 156 (2009) 697 – 705.
- [18] T. Blacha, M. Di Domenico, P. Gerlinger, M. Aigner, Soot predictions in premixed and non-premixed laminar flames using a sectional approach for pahs and soot, *Combust. Flame* 159 (2012) 181–193.
- [19] C. Eberle, P. Gerlinger, M. Aigner, A sectional PAH model with reversible PAH chemistry for cfd soot simulations, *Combust. Flame* 179 (2017) 63–73.
- [20] M. Frenklach, S. J. Harris, Aerosol dynamics modeling using the method of moments, *J. Colloid Interface Sci.* 118 (1987) 252–261.
- [21] G. Blanquart, H. Pitsch, A joint volume-surface-hydrogen multi-variate model for soot formation, in: *Combustion Generated Fine Carbonaceous Particles*, Henning Bockhorn, 2007, pp. 437–463.
- [22] M. E. Mueller, G. Blanquart, H. Pitsch, A joint volume-surface model of soot aggregation with the method of moments, *Proc. Combust. Inst.* 32 (2009) 785 – 792.

- [23] S. Salenbauch, C. Hasse, M. Vanni, D. L. Marchisio, A numerically robust method of moments with number density function reconstruction and its application to soot formation, growth and oxidation, *J. Aerosol Sci.* 128 (2019) 34 – 49.
- [24] P. A. Tesner, T. D. Smegiriova, V. G. Knorre, Kinetics of dispersed carbon formation, *Combust. Flame* 17 (1971) 253–260.
- [25] J. B. Moss, C. D. Stewart, K. J. Syed, Flowfield modelling of soot formation at elevated pressure, *Symp. (Int.) Combust.* 22 (1989) 413–423.
- [26] K. M. Leung, R. P. Lindstedt, W. P. Jones, A simplified reaction mechanism for soot formation in nonpremixed flames, *Combust. Flame* 87 (1991) 289–305.
- [27] B. Franzelli, A. Vié, N. Darabiha, A three-equation model for the prediction of soot emissions in les of gas turbines, *Proc. Combust. Inst.* 37 (2019) 5411 – 5419.
- [28] M. Jadidi, S. Kostic, L. Zimmer, S. B. Dworkin, An artificial neural network for the low-cost prediction of soot emissions, *Energies* 13 (2020) 4787.
- [29] M. Jadidi, L. Di Liddo, S. B. Dworkin, A long short-term memory neural network for the low-cost prediction of soot concentration in a time-dependent flame, *Energies* 14 (2021) 1394.

- [30] M. Cailler, N. Darabiha, D. Veynante, B. Fiorina, Building-up virtual optimized mechanism for flame modeling, *Proc. Combust. Inst.* 36 (2017) 1251 – 1258.
- [31] M. Cailler, N. Darabiha, B. Fiorina, Development of a virtual optimized chemistry method. Application to hydrocarbon/air combustion, *Combust. Flame* 211 (2020) 281 – 302.
- [32] G. Maio, M. Cailler, R. Mercier, B. Fiorina, Virtual chemistry for temperature and CO prediction in LES of non-adiabatic turbulent flames, *Proc. Combust. Inst.* 37 (2019) 2591 – 2599.
- [33] G. Maio, M. Cailler, A. Cuoci, B. Fiorina, A virtual chemical mechanism for prediction of NO emissions from flames, *Combust. Theory Model.* 24 (2020) 872–902.
- [34] R. J. Santoro, H. G. Semerjian, R. A. Dobbins, Soot particle measurements in diffusion flames, *Combust. Flame* 51 (1983) 203–218.
- [35] C. A. Schuetz, M. Frenklach, Nucleation of soot: Molecular dynamics simulations of pyrene dimerization, *Proc. Combust. Inst.* 29 (2002) 2307 – 2314.
- [36] P. Selvaraj, P. G. Arias, B. J. Lee, H. G. Im, Y. Wang, Y. Gao, S. Park, S. M. Sarathy, T. Lu, S. H. Chung, A computational study of ethylene–air sooting flames: Effects of large polycyclic aromatic hydrocarbons, *Combust. Flame* 163 (2016) 427–436.

- [37] B. Fiorina, O. Gicquel, L. Vervisch, S. Carpentier, N. Darabiha, Premixed turbulent combustion modeling using tabulated detailed chemistry and pdf, *Proc. Combust. Inst.* 30 (2005) 867–874.
- [38] R. Barlow, A. Karpetis, J. Frank, J.-Y. Chen, Scalar profiles and no formation in laminar opposed-flow partially premixed methane/air flames, *Combust. Flame* 127 (2001) 2102–2118.
- [39] M. F. Modest, *Radiative Heat Transfer (Third Edition)*, Academic Press, Boston, 2013.
- [40] W. Pejpichestakul, A. Cuoci, A. Frassoldati, M. Pelucchi, A. Parente, T. Faravelli, Buoyancy effect in sooting laminar premixed ethylene flame, *Combust. Flame* 205 (2019) 135 – 146.
- [41] A. Soufiani, J. Taine, Application of statistical narrow-band model to coupled radiation and convection at high temperature, *Int. J. Heat Mass Transf.* 30 (1987) 437–447.
- [42] N. Darabiha, S. Candel, The influence of the temperature on extinction and ignition limits of strained hydrogen-air diffusion flames, *Combust. Sci. Technol.* 86 (1992) 67–85.
- [43] A. V. Menon, S.-Y. Lee, M. J. Linevsky, T. A. Litzinger, R. J. Santoro, Addition of no<sub>2</sub> to a laminar premixed ethylene–air flame: effect on soot formation, *Proc. Combust. Inst.* 31 (2007) 593–601.
- [44] F. Xu, P. B. Sunderland, G. M. Faeth, Soot formation in laminar premixed ethylene/air flames at atmospheric pressure, *Combust. Flame* 108 (1997) 471–493.

- [45] ISF5, International sooting flame workshop, <http://www.adelaide.edu.au/cet/isfworkshop/data-sets/>, 2021.
- [46] A. Cuoci, A. Frassoldati, T. Faravelli, E. Ranzi, Numerical modeling of laminar flames with detailed kinetics based on the operator-splitting method, *Energy & fuels* 27 (2013) 7730–7753.
- [47] A. Cuoci, A. Frassoldati, T. Faravelli, E. Ranzi, A computational tool for the detailed kinetic modeling of laminar flames: Application to c2h4/ch4 coflow flames, *Combust. Flame* 160 (2013) 870–886.
- [48] A. L. Bodor, B. Franzelli, T. Faravelli, A. Cuoci, A post processing technique to predict primary particle size of sooting flames based on a chemical discrete sectional model: Application to diluted coflow flames, *Combust. Flame* 208 (2019) 122 – 138.
- [49] R. Santoro, T. Yeh, J. Horvath, H. Semerjian, The transport and growth of soot particles in laminar diffusion flames, *Combust. Sci. Technol.* 53 (1987) 89–115.
- [50] M. Di Domenico, P. Gerlinger, M. Aigner, Development and validation of a new soot formation model for gas turbine combustor simulations, *Combust. Flame* 157 (2010) 246–258.
- [51] P. Akridis, S. Rigopoulos, Modelling of soot formation in laminar diffusion flames using a comprehensive cfd-pbe model with detailed gas-phase chemistry, *Combust. Theory Model.* 21 (2017) 35–48.
- [52] H. Wang, A. Laskin, A comprehensive reaction model of ethylene and

- acetylene combustion, URL: <http://ignis.usc.edu/Mechanisms/C2-C4/c2.html> (2000).
- [53] F. Liu, H. Guo, G. J. Smallwood, O. L. Gülder, Numerical modelling of soot formation and oxidation in laminar coflow non-smoking and smoking ethylene diffusion flames, *Combust. Theory Model.* 7 (2003) 301–315.
- [54] M. D. Smooke, M. B. Long, B. C. Connelly, M. B. Colket, R. J. Hall, Soot formation in laminar diffusion flames, *Combust. Flame* 143 (2005) 613–628.
- [55] R. Hall, M. Smooke, M. Colket, Predictions of soot dynamics in opposed jet diffusion flames, *Physical and Chemical Aspects of Combustion: A Tribute to Irvin Glassman* 4 (1997) 189–229.
- [56] A. Kronenburg, R. W. Bilger, J. H. Kent, Modeling soot formation in turbulent methane–air jet diffusion flames, *Combust. Flame* 121 (2000) 24–40.
- [57] J. Bonnety, A. Guibaud, R. Jalain, A. Matynia, J.-L. Consalvi, F. Liu, G. Legros, Probing the local radiative quenching during the transition from a non-smoking to a smoking laminar coflow ethylene/air non-premixed flame, *Combustion and Flame* 203 (2019) 120–129.